
IEEE Copyright Notice

© 2023 IEEE.

Personal use of this material is permitted. Permission from IEEE must be obtained for all other uses, in any current or future media, including reprinting/republishing this material for advertising or promotional purposes, creating new collective works, for resale or redistribution to servers or lists, or reuse of any copyrighted component of this work in other works.

arXiv:2302.13819v2 [astro-ph.IM] 1 Mar 2023

Performance analysis of sequential carrier- and code-tracking receivers in the context of high-precision space-borne metrology systems

PHILIPP EURINGER¹, GERALD HECHENBLAIKNER¹, FRANCIS SOUALLE², AND WALTER FICHTER³

¹*Airbus Space Systems, Airbus Defence and Space GmbH, Claude-Dornier-Straße, 88090 Immenstaad am Bodensee, Germany*

²*Airbus Space Systems, Airbus Defence and Space GmbH, Willy-Messerschmitt-Straße 1, 82024 Taufkirchen, Germany*

³*Institute of Flight Mechanics and Control, University of Stuttgart, Pfaffenwaldring 27, 70569 Stuttgart, Germany*

Future space observatories achieve detection of gravitational waves by interferometric measurements of a carrier phase, allowing to determine relative distance changes, in combination with an absolute distance measurement based on the transmission of pseudo-random noise chip sequences. In addition, usage of direct-sequence spread spectrum modulation enables data transmission. Hereafter, we report on the findings of a performance evaluation of planned receiver architectures, performing phase and distance readout sequentially. An analytical model is presented identifying the power spectral density of the chip modulation at frequencies within the measurement bandwidth as the main driver for phase noise. This model, verified by numerical simulations, excludes binary phase-shift keying modulations for missions requiring pico-meter noise levels at the phase readout, while binary offset carrier modulation, where most of the power has been shifted outside the measurement bandwidth, exhibits superior phase measurement performance. Ranging analyses of the delay-locked loop reveal strong distortion of the pulse shape due to the preceding phase tracking introducing ranging bias variations. Numerical simulations show that these variations, however, originating from data transitions, are compensated by the delay tracking loop and are thus not considered critical, irrespective of the modulation type.

1 Introduction

1.1 High-precision space-borne metrology systems

Recent years have seen rapid advancements in missions using optical interferometry in space. Some missions, such as Grace FO [1] and the planned NGGM mission [13], monitor spatial and long-term temporal variations of the Earth's gravitational field. To this end, optical interferometers are used to measure the relative distance changes between two satellites which are separated by approximately 100 km and therefore experience slightly different gravitational accelerations. Non-gravitational accelerations can be compensated in post-processing through accelerometer measurements performed on both satellites.

Other missions, such as the planned space observatories LISA [7] (Europe/US), TAIJI [17] and TIANQIN [18] (China), and DECIGO [16] (Japan), aim to detect gravitational waves by interferometric measurements across huge distances of up to several million kilometers in order to achieve the required strain sensitivity on the order of 1 part in 10^{20} .

LISA is a planned ESA/NASA mission, currently in Phase B1 of the development, with a constellation of 3 spacecraft (SC) forming an equilateral triangle of 2.5 million km arm-length. Two one-way optical links are established in opposing directions between each pair of SC. These are primarily used for interferometric measurements of the carrier phase to determine relative distance changes with an accuracy of approximately $10 \text{ pm}/\sqrt{\text{Hz}}$ in a measurement bandwidth from 0.1 mHz to 1 Hz [6]. However, as a secondary function, the links also allow determining the absolute distance (ranging) and exchanging data in between SC by modulating pseudo-random noise (PRN) sequences onto the carrier and data bits onto the PRN code sequences [14, 21].

Knowledge of the absolute distance is obtained by correlating the received PRN code sequence with a local SC replica, which yields the relative code delays and the associated inter-SC distance within an ambiguity range, in a similar way as done in the radio frequency domain by global navigation satellite systems (GNSS). The ambiguity can then be resolved by a combination of radio-frequency ranging measurements from ground stations and orbit prediction between measurements [6].

For LISA, accurate knowledge of the inter-SC distance is needed for a post-processing technique referred to as time-delay-interferometry [22]. Thereby, virtual Michelson interferometers are synthesized from individual arm measurements in order to suppress laser frequency noise [19] and tilt-to-length coupling noise [15] by several orders of magnitude. Aforementioned Earth observation missions, GRACE FO and NGGM, do not strictly rely on inter-SC distance measurements, however, in order to map the Earth's gravitational field with high accuracy, the positions of the individual SC must be precisely known. This currently requires the use of GNSS receivers and ground-station-based laser ranging [13] to support the precise orbit prediction, which would additionally benefit from ranging information in between the SC.

In this paper, we investigate the performance of optical metrology systems used for interferometry as a primary function combined with laser ranging and data transfer as a secondary function, as planned for future missions in space. One of the possible phase detection architectures employs a phase-locked loop (PLL), used for measuring the interferometric phase, sequentially followed by a delay-lock-loop (DLL), used for measuring the code delay to determine the range. This simple architecture saves costs and resources, in particular also

computational effort and power dissipation (which impacts thermal stability), compared to more complex architectures. However, phase measurement performance may be antagonistic to ranging accuracy and vice versa, which requires the correct choice of modulation type and signal processing parameters, as we will see in the discussions below.

1.2 Signal composition and receiver architecture

The signal model of Eq. 1 will be used for the performance assessment in the following sections. It has modulation features that support an absolute distance measurement combined with a high-precision but ambiguous carrier measurement and may represent the output of a heterodyne detection pre-processing step, as detailed in [8, 9].

$$s(t) = \cos \left(\omega t + m_{\text{prn}} \sum_{j=-\infty}^{\infty} d_j \sum_{i=0}^{N-1} c_i p(t - iT_c - jNT_c) \right). \quad (1)$$

The first argument in the cosine represents the carrier phase of the incoming signal, given by the angular frequency ω and the time t . The second argument carries a chip sequence, commonly known as PRN, enabling absolute ranging, where the chip sequence consists of N chips with a chip period T_c . Here, $c_i \in \{\pm 1\}$ and $p(t)$ represent the chip value of the i -th chip and the pulse modulation, respectively. Thus, the pulse modulation can carry any function in the range from t to $t + T_c$, outside this range it reads zero. In addition, the chip sequence is modulated with a binary symbol ($d_j \in \{\pm 1\}$), with period $T_s = NT_c$, for data transmission. Importantly, the modulation depth is controlled by the parameter m_{prn} , known as modulation index. In this sense, only parts of the carrier signal are modulated by the chip sequence [11].

Contrary to typical GNSS architectures, high-precision optical metrology systems have a strong emphasis on the phase measurement, which requires decoupling of code and phase estimation in order to avoid disturbance effects of the DLL onto the PLL. This suggests using a sequential PLL–DLL architecture, as proposed by Delgado [8, 10, 11]. The advantage of this cascaded architecture is a reduction of the receiver complexity with separation of individual tracking functions into single components. A generic model following this approach is illustrated in Fig. 1. The receiver consists of two main components: the PLL and the DLL being responsible for the carrier tracking, i.e. the phase readout, and code tracking, i.e. the absolute ranging, respectively. The PLL represents a second-order all-digital PLL consisting of a phase detector, a first-order filter and a numerically controlled oscillator (NCO). This generic design is studied extensively in several textbooks [12, 20], and based on linear transfer models, it exhibits a low-pass filter behavior in its closed-loop response, while the error response filter yields a high-pass filter behavior [12]. Thus the general principle is as follows: Presuming that the error response bandwidth of the PLL is smaller than the chip rate, the PLL is not able to track chip fluctuations, and the chip sequences will remain in the error channel of the PLL. Consequently, the error channel of the PLL serves as an input to the DLL, cf. Fig. 1. The DLL estimates the time of arrival (TOA) of the incoming PRN sequence based on an early-late discriminator, while a prompt channel is used for data retrieval. The output of the early-late discriminator is thereby low-pass filtered, yielding an update of the TOA for the PRN code generator.

Finally, Tab. 1 lists parameters derived from the generic model delineated in Fig. 1. Parameter values have been taken from tables listed in [8] and derived from [11], and where necessary, values not included were added to the table. Thus, these values are regarded as relevant within high-precision space-borne metrology systems, in particular LISA.

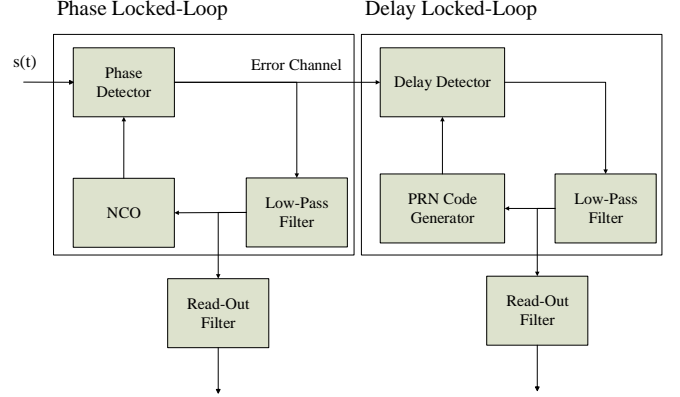


Fig. 1. The incoming signal $s(t)$ is processed by an all-digital second-order PLL, followed by a first-order DLL with a non-coherent early-late discriminator for the ranging, and a prompt channel for data retrieval (not shown). A similar model derived from control loop theory is applied to both tracking loops with a detector, a low pass filter and a reference signal generator. The output at the PLL read-out filter is a frequency estimate, while the read-out of the DLL is a chip rate estimate.

Parameter (Unit)	Symbol	Value
Modulation index (-)	m_{prn}	0.1
Chip period (ms)	T_c	0.001
Sampling rate (MHz)	f_s	80
Symbol period (ms)	T_s	0.064
Carrier frequency (Mrad/s)	ω	30π
PLL bandwidth (closed loop) (kHz)	B_{PLL}	250
PLL bandwidth (error loop) (kHz)	B_{PLL}	250
DLL bandwidth (closed loop) (Hz)	B_{PLL}	10
Read-out filter PLL (Hz)	B_{F}^{p}	4
Read-out filter DLL (Hz)	B_{F}^{d}	10
BPSK early-late spacing (T_c)	Δ_{BPSK}	0.5
BOC(1,1) early-late spacing (T_c)	Δ_{BOC}	0.2
Wavelength at heterodyne detection (nm)	λ	1064

Table 1. Baseline parameters

1.3 Motivation and delimitation

The simple receiver design as delineated in section 1.2, offers great advantages regarding manufacturing, complexity and testing, thanks to its modular design. However, as explained later, the simplicity of the architecture affects the performance of the receiver. Thus, a model will be set up specifically for each core function, namely carrier and code tracking, providing in-depth insight into the performance during signal tracking. Moreover, these models will identify key performance drivers enabling even such simple receiver architectures are in principle mature enough for precise length measurements, once certain requirements are met (in particular on the pulse modulation).

The models introduced here below represent a generic case. However, due to its generality, it is easy to apply the models to more specific cases, which will be discussed in the respective sections.

The structure of the paper will be as follows: The focus of section 2 is on the interferometric measurement performance. Thereby, the phase noise resulting from the architecture and the signal composition will be identified and modeled, yielding an analytic expression. This expression will be applied to two typical modulation schemes and compared to the result of a numerical breadboard setup in MATLAB. We find that the simplest of the previously considered modulation schemes (binary phase-shift keying, [10, 14]) degrades the primary phase measurement accuracy to unacceptable levels, while performance is fully recovered when adopting an alternative modulation scheme, namely binary offset carrier modulation. The ranging accuracy of these two modulation schemes is assessed in section 3, where we find that both schemes can easily achieve the required performance with comparable accuracy.

2 Carrier tracking and phase read-out performance

2.1 Signal modeling

The measured carrier phase must be of the highest possible accuracy in order to determine relative inter-SC distance changes. As shown in Eq. 1, the chip sequence will contribute to the phase measurement noise. Thereby, the data symbol values are not predefined and can be modeled as a random stream. In contrast, the chip values are predefined and follow a fixed pattern. Nevertheless, for sufficiently long PRN sequences, the chip stream will be considered random for the sake of the following development. Consequently, both variables may be modeled as Bernoulli variables $\hat{C}_i, \hat{D}_j \in \{\pm 1\}$, motivating the introduction of a new Bernoulli variable $\hat{C}_i \hat{D}_j \rightarrow \hat{X}_{ij} \in \{\pm 1\}$. Thus, the expression for the resulting stochastic noise term $\hat{n}(t)$ is given by:

$$\hat{n}(t) = m_{\text{prn}} \sum_{n=-\infty}^{\infty} \hat{X}_n p(t - nT_c). \quad (2)$$

Noting that the pulse modulation $p(t)$ is independent of the index n , the former can be expressed according to:

$$\hat{n}(t) = m_{\text{prn}} \sum_{n=-\infty}^{\infty} \hat{X}_n \delta(t - nT_c) * p(t), \quad (3)$$

$$= \hat{g}(t) * p(t), \quad (4)$$

where $*$ denotes the convolution operator. In the following section, this term will be used for the calculation of the phase noise measurement performance.

2.2 Phase noise

Phase noise is commonly measured as a power spectral density (PSD) $S(f)$, where the variance σ^2 of phase noise can be deduced from. Modeling the PLL as a linear time-invariant (LTI) system and taking

into account the processing according to Fig. 1, the PSD at the readout is given by the noise power spectral density $N(f)$ at the input of the PLL filtered by the closed-loop transfer function of the PLL $H_{\text{PLL}}(f)$ and the read-out filter $H_{\text{F}}(f)$ [12]. Since the sampling rate (80 MHz) of the PLL is significantly larger than its closed-loop bandwidth (250 kHz), the system can be well approximated by a continuous representation in the frequency domain [20]. Both, the closed-loop PLL and the read-out filter exhibit a low-pass filter behavior and may be idealized according to $|H_x(f)| = \Pi_{-B_x, B_x}(f)$. Hereby, the boxcar function $\Pi(f)$ is defined via the Heaviside step function $\theta(t)$, according to: $\Pi_{a,b}(f) = \theta(f - a) - \theta(f - b)$. Noting that the closed-loop bandwidth of the B_{PLL} (250 kHz) exceeds the bandwidth of the read-out filter B_{F}^{p} (Hz – kHz) by orders of magnitude, results in a PSD and the corresponding variance at the readout of:

$$S(f) = \Pi_{-B_{\text{PLL}}, B_{\text{PLL}}}(f) \Pi_{-B_{\text{F}}, B_{\text{F}}}(f) N(f) \approx \Pi_{-B_{\text{F}}^{\text{p}}, B_{\text{F}}^{\text{p}}}(f) N(f), \quad (5)$$

$$\sigma^2 \approx \int_{-B_{\text{F}}^{\text{p}}}^{B_{\text{F}}^{\text{p}}} N(f) df. \quad (6)$$

Thereby, Eq. 5 denotes the double-sided PSD, which will be used in the remainder of this paper. In addition, introducing the Fourier pairs $\hat{g}(t) \xrightarrow{\mathcal{F}} \hat{G}(f)$, $p(t) \xrightarrow{\mathcal{F}} P(f)$ and $\hat{n}(t) \xrightarrow{\mathcal{F}} \hat{N}(f)$ and exploiting the convolution theorem on Eq. 4 yields $\hat{N}(f) = \hat{G}(f) \cdot P(f)$. Thus the noise power spectral density at the input of the PLL is given by:

$$\begin{aligned} N(f) &= \lim_{K \rightarrow \infty} \frac{1}{2KT_c} \langle |\hat{N}(f)|^2 \rangle, \\ &= \frac{|P(f)|^2}{2T_c} \lim_{K \rightarrow \infty} \frac{\langle |\hat{G}(f)|^2 \rangle}{K}, \\ &= \frac{|P(f)|^2}{2T_c} \lim_{K \rightarrow \infty} \frac{m_{\text{prn}}^2}{K} \sum_{m,n=-K}^{K-1} \langle \hat{X}_n \hat{X}_m \rangle e^{i2\pi f(n-m)T_c}, \\ &= m_{\text{prn}}^2 \frac{|P(f)|^2}{T_c} \left[1 + \lim_{K \rightarrow \infty} \frac{1}{2K} \sum_{\substack{m,n=-K \\ m \neq n}}^{K-1} \langle \hat{X}_n \hat{X}_m \rangle e^{i2\pi f(n-m)T_c} \right]. \end{aligned} \quad (7)$$

Thereby, the brackets $\langle \rangle$, indicate the ensemble average over the Bernoulli variables \hat{X}_n and \hat{X}_m . If \hat{X}_n and \hat{X}_m are uncorrelated for $n \neq m$, the noise power spectral density is solely given by the PSD of the pulse modulation multiplied by the modulation index squared. In this limit, inserting Eq. 7 into Eq. 5 and Eq. 6 yields:

$$S(f) = \Pi_{-B_{\text{F}}^{\text{p}}, B_{\text{F}}^{\text{p}}}(f) m_{\text{prn}}^2 \frac{|P(f)|^2}{T_c}, \quad (8)$$

$$\sigma^2 = m_{\text{prn}}^2 \int_{-B_{\text{F}}^{\text{p}}}^{B_{\text{F}}^{\text{p}}} \frac{|P(f)|^2}{T_c} df. \quad (9)$$

Equations 8 and 9 highlight the impact of the PSD of the pulse modulation on the phase noise performance, which is further quantified in the following section.

2.3 Application and numerical verification

Typical types of pulse modulation schemes are binary phase shift keying (BPSK) and binary offset carrier (BOC). In this discussion, we will restrict ourselves specifically to BPSK-R (where the R indicates a rectangular pulse modulation) and sine-phased BOC(m,n), with $m/n \in \mathbb{N}$. For a BPSK-R modulation with chip period T_c , the PSD is given by: $|P_{\text{BPSK}}(f)|^2/T_c = T_c \text{sinc}^2(\pi f T_c)$, with $\text{sinc}(x) = \sin(x)/x$. Notably, this function exhibits a maximum at the origin, i.e. at frequencies not being filtered at the phase read-out, cf. gray graph in Fig. 2 a).

Inserting the PSD of the pulse modulation into Eq. 8 and Eq. 9 results in:

$$S_{\text{BPSK-R}}(f) = \Pi_{-B_F^p, B_F^p}(f) m_{\text{prn}}^2 T_c \text{sinc}^2(\pi f T_c), \quad (10)$$

$$\approx \Pi_{-B_F^p, B_F^p}(f) m_{\text{prn}}^2 T_c, \quad (11)$$

$$\sigma_{\text{BPSK-R}}^2 = m_{\text{prn}}^2 \int_{-B_F^p}^{B_F^p} T_c \text{sinc}^2(\pi f T_c) df, \quad (12)$$

$$\approx 2m_{\text{prn}}^2 B_F^p T_c. \quad (13)$$

Thereby, the sine cardinal has been approximated using a Taylor expansion according to $\text{sinc}(x) \approx 1$, as $B_F^p \ll 1/T_c$. Importantly, the PSD of the phase noise exhibits a constant value at low frequencies. Thus, the phase noise can only be reduced via the chip period and the modulation index. However, when reducing the modulation index to a level where the residual phase noise becomes acceptable, the code tracking and associated ranging error, discussed in the subsequent section, may become in-acceptably large. Similarly, a smaller chip period may shift large parts of the spectral energy of the modulation outside the receiver measurement bandwidth. This situation can however be improved when applying modulation schemes such as BOC, as shown hereafter.

First introduced by John Betz, BOC(m,n) is characterized by a square sub-carrier modulation of the chips [3]. The frequency f_{sc} of the sub-carrier is expressed by the index $m = f_{sc}/f_{\text{ref}}$, where f_{ref} represents a reference frequency. The second index $n = f_c/f_{\text{ref}}$ defines the chip rate f_c . As we restricted the signal to exhibit a constant pulse modulation $p(t)$, cf. Eq. 1, it is necessary to have a sub-carrier multiple of the chip rate, yielding $m/n \in \mathbb{N}$. With no loss of generality, we set $f_c = f_{\text{ref}}$, expressed as $n = 1$. Following these presumptions, the PSD of the sine-phased BOC($m,1$) is given by $|P_{\text{BOC}(m,1)}(f)|^2/T_c = T_c \text{sinc}^2(\pi f T_c) \tan^2(\pi f T_c / (2m))$ [3]. In strong contrast to BPSK, the peak of the PSD is shifted away from the origin, to $f \approx \pm f_{sc}$. Moreover, the power contribution at the origin reads zero, cf. blue graph in Fig. 2 a). Finally, performing similar approximations as for the BPSK modulation results in a phase noise PSD and variance of:

$$S_{\text{BOC}(m,1)}(f) = \Pi_{-B_F^p, B_F^p}(f) m_{\text{prn}}^2 T_c \text{sinc}^2(\pi f T_c) \tan^2\left(\frac{\pi f T_c}{2m}\right), \quad (14)$$

$$\approx \Pi_{-B_F^p, B_F^p}(f) m_{\text{prn}}^2 T_c^3 \left(\frac{\pi f}{2m}\right)^2, \quad (15)$$

$$\sigma_{\text{BOC}(m,1)}^2 = m_{\text{prn}}^2 \int_{-B_F^p}^{B_F^p} T_c \text{sinc}^2(\pi f T_c) \tan^2\left(\frac{\pi f T_c}{2m}\right) df, \quad (16)$$

$$\approx \left(\frac{\pi m_{\text{prn}}}{m}\right)^2 \frac{(B_F^p T_c)^3}{6}. \quad (17)$$

Strikingly, and in strong contrast to BPSK modulation, the phase noise PSD for BOC($m,1$) reads zero at the origin and increases quadratically. Consequently, $S_{\text{BOC}(m,1)}(f)$ exhibits a maximum at $f = B_F^p$. The ratio at this maximum between BOC($m,1$) and BPSK modulation is $(B_F^p T_c \pi / 2m)^2$. Thus as long as $B_F^p T_c \ll 1$, which generally holds for most baseline configurations, cf. Tab. 1, BOC($m,1$) modulation exhibits superior noise performance compared to BPSK modulation. A similar conclusion holds for the variance.

The striking benefit of BOC(1,1) over BPSK regarding the phase noise gets especially visible once relevant parameter values foreseen for the space-borne metrology system LISA are taken into account, see Tab. 1. In this context the phase read-out accuracy is analyzed in terms of displacement noise. For this purpose, the phase noise is considered as linear spectral density (LSD), obtained via the square

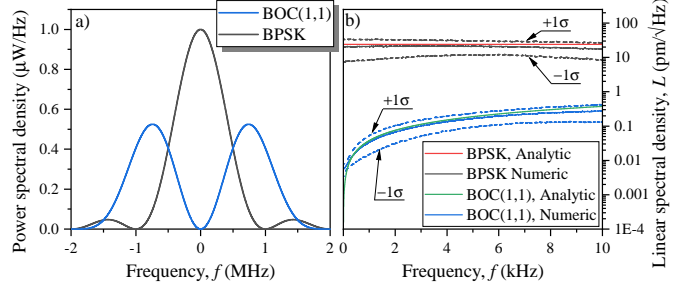


Fig. 2. Panel a) illustrates the double-sided PSD for a BPSK (gray graph) and BOC(1,1) (blue graph) modulated rectangular chip, exhibiting a chip width of 0.001 ms. In panel b) the single-sided phase noise LSD of a numerical PLL simulation (gray lines for BPSK and blue lines for BOC) and an analytical model (red line for BPSK and green line for BOC) are compared, based on the parameter values of Tab. 1. Within the numerical simulation 32 randomly generated chip sequences have been considered. Thereby, the mean value (solid lines) and the one-sigma interval (dashed lines) are depicted after smoothing.

root of the PSD. Converting the phase noise into displacement noise by multiplication with the conversion factor $\lambda/(2\pi)$, where λ denotes the wavelength at the heterodyne detection, yields a single-sided LSD $L(f) = \sqrt{2S(f)} \lambda/(2\pi)$ in $\text{m}/\sqrt{\text{Hz}}$, which for BPSK modulation exceeds the BOC(1,1) LSD by five orders of magnitude.

This significant difference is verified by a numerical PLL simulation, set up according to the generic model depicted in Fig. 1 and parameter values listed in Tab. 1. Thereby, 32 randomly generated PRN sequences, modulated either via BPSK (gray lines) or BOC(1,1) (blue lines) have been considered. Figure 2 b) illustrates the single-sided LSD $L(f)$ of the phase noise, where the mean value (solid lines) and the one-sigma interval (dashed lines) are depicted after smoothing. Both numerical simulations agree well with the respective analytical model, exhibiting a constant slope for the LSD of the BPSK modulation and a linear one for the BOC(1,1) modulation. Deviations from the analytical model are attributed to the finite chip sequence length and are found to vanish for infinitely long sequences. Importantly, these results manifest the superior phase noise performance of the BOC(1,1) modulation. On the other hand, they exclude BPSK modulation for the given set of parameter values for applications requiring picometer phase noise levels.

This result will generally hold also in the presence of thermal noise as long as the chip modulation is the dominating noise contribution considering the phase read-out. Moreover, without data transmission, the signal consists of only periodical spreading sequences, which yield in the frequency domain a comb around the origin spaced by the inverse of the code sequence periodicity. Since $B_F^p \ll 1/T_s$, only the peak at the origin may affect the result, which in the case of a BOC($m,1$) modulation is suppressed, due to the symmetry properties of the pulse.

3 Code tracking and ranging performance

3.1 Principle of DLL

After carrier wiping, a DLL relying on the principle of a non-coherent early-late discriminator, and extensively used in GNSS applications, is capable of tracking the code according to Eq. 1. Thereby, the principle of the delay detector, see Fig. 1, relies on two local code replicas – forwarded and delayed in time, where the particular delay of the code replicas, i.e. the early-late spacing, depends strongly on the modulation technique [2, 23]. These replicas are correlated with the incoming

signal over one symbol period, followed by a squared magnitude operation, to suppress data polarity. Finally, the difference between early and late correlation yields a value on the so-called S-curve $S(\varepsilon)$. Thereby, the argument ε indicates the time shift between the replica and the incoming signal. The gray curve in Fig. 3 b) illustrates a S-curve for an exemplary BPSK-modulated incoming chip sequence which equals its replica. A time segment of the incoming signal, and thus of the replica, is depicted in Fig. 3 a) by the gray curve. For this ideal incoming signal, the zero crossing corresponds to perfect alignment between replica and incoming signal, and is usually considered as the tracking point of the loop, with a tracking range corresponding to the linear regime around the zero crossing. In addition, the blue graph in Fig. 3 b) depicts the S-curve for a BOC(1,1)-modulated signal and its identical replica, whose time segment is portrayed in Fig. 3 b), also by the blue graph. In contrast to the BPSK-modulated S-curve, there are additional stable tracking points, represented by additional zero-crossings within a region of positive slope. These play a key role during loop (re-)acquisition but are not further elaborated in the following discussion. Moreover, the linear range is reduced, due to the necessarily smaller early-late spacing, cf. Tab. 1. Irrespective of the modulation, within the linear range, the time shift between the replica and the incoming signal is obtained via the division of the S-curve value by the constant slope $m = \partial_\varepsilon S$ in this regime. In this context, the slope is usually represented as a discriminator gain $d_g = 1/m$ [2]. Finally, this shift serves as an input to the low-pass filter, which estimates the chip rate used as input to the PRN code generator.

3.2 Signal modeling

In strong contrast to the ideal, i.e. unfiltered, case stated in section 3.1, the architecture depicted in Fig. 1, not only wipes the carrier but also affects the code sequences. Based on standard control theory the code sequences are filtered by the impulse response of the error transfer function $e(t)$ of the PLL, yielding the signal $\tilde{s}(t) = e(t) * m_{\text{prn}} \sum_{j=-\infty}^{\infty} d_j \sum_{i=0}^{N-1} c_i p(t - iT_c - jNT_c)$, at the input of the DLL. Taking into account the high-pass filter behavior of the error transfer function and the PSD of the two modulation methods, cf. Fig. 2 a), we find that BPSK-modulated sequences are significantly more distorted than BOC(1,1)-modulated sequences. This behavior is illustrated by the red and green curves of Fig 3 a), for BPSK and BOC(1,1) modulation, respectively, which constitute the filtered signals used as input to the DLL. Nonetheless, both signals are characterized by overshoots at the beginning of a chip value transition and strong damping toward the end of the chip. As a consequence, the resulting S-curves, based on the correlation of the filtered signal with an unfiltered replica, differ significantly from the ideal case. In particular, for BPSK modulation, cf. red graph in Fig 3 b), the distortion leads to additional stable tracking points. Besides the shape also the zero crossing of the linear range, i.e. the primary tracking point, is shifted by nearly one chip period, which will be referred to as ranging bias [4]. For BOC(1,1) modulation, alternation in shape and zero crossing are moderate, cf. green graph in Fig 3 b).

Moreover, due to the convolution operation of the filtering, i.e. due to the filter memory, the symbols not only differ in sign, which is well accounted for by the magnitude (squared) operation but rather they depend on the input of the previous symbols. Consequently, the corresponding S-curve varies over time, yielding a ranging bias variation.

As a matter of fact, analyzing an uncorrelated chip sequence after exposure to a high-pass filter, representative for the error transfer function of the PLL, reveals a correlation time limited to several chip periods. This behavior is observed for BPSK and BOC(1,1) modulation for a bandwidth (BW) of 10 - 500 kHz, cf. Fig. 4 panel d), which appears as relevant PLL bandwidth range considering a chip rate of

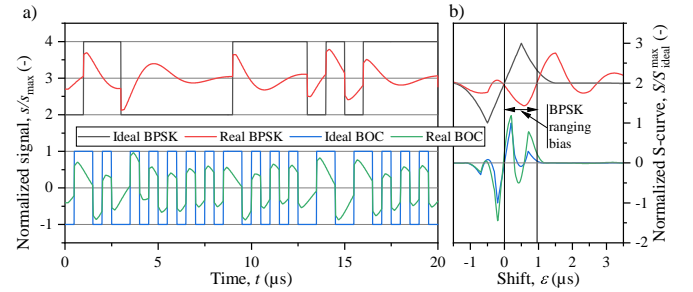


Fig. 3. Panel a) illustrates exemplary time segments of BPSK- and BOC(1,1)-modulated chip sequences. Thereby, the signals $s(t)$ are normalized to their maximum value s_{max} and represent an ideal, i.e. unfiltered, incoming wide-band signal (gray graph) and the real, i.e. filtered by the PLL, incoming signal (red graph) for BPSK modulation. Similarly, for BOC(1,1) modulation unfiltered and filtered signals are depicted by the blue and green graphs, respectively. In addition, the BPSK-modulated signals are shifted for clarity by $s/s_{\text{max}} = 3$. The corresponding S-curves for the replica and the ideal signal (gray curve for BPSK and blue curve for BOC), as well as for the replica and the real signal (red curve for BPSK and green curve for BOC) are presented in panel b). Thereby, the S-curves are normalized to the maximum value of the ideal S-curve. The S-curves based on the real signals differ in shape and also in the zero crossing of the linear range compared to the S-curves based on the ideal signals. The shift of the zero-crossing is thereby denoted as ranging bias, exemplary indicated for BPSK modulation by the black double arrow. Again, the BPSK-modulated S-curves are offset for clarity by $S/S_{\text{ideal}}^{\text{max}} = 2$.

1 MHz. These findings exclude the persistence of correlation over more than one symbol length (64 chips, cf. Tab. 1). Therefore, a symbol and its modulated data bit can have at most an impact on the processing of the succeeding symbol and data bit (memory effect). In addition, these findings are affirmed by numerical analysis based on randomly generated PRN sequences and parameter values stated in Tab. 1, revealing that variations of the S-curve are restricted to S^+ and S^- , depending on whether the current and previous data symbols exhibit the same (+) or opposite (-) value. These S-curves, depicted in Fig. 4 a) for an exemplary BPSK-modulated PRN sequence, promote the introduction of a mean S-curve $S(\bar{\varepsilon})$ in the linear range, exhibiting a mean ranging bias \bar{b} as portrayed in Fig. 4 b). Importantly, $\bar{\varepsilon} = [\varepsilon(S^+) + \varepsilon(S^-)]/2$ indicates the mean value based on the x-axis, which can be found via interpolation of $S^\pm(\varepsilon)$ in the linear range of S^+ and S^- . This leads to a common offset Δb between the mean S-curve $S(\bar{\varepsilon})$ and S^\pm at the zero crossing. Consequently, the ranging bias can be modeled as:

$$b(t) = \Delta b \sum_{n=-\infty}^{\infty} \hat{f}_n \Pi_{nT_s, (n+1)T_s}(t) + \bar{b}.$$

Thereby, the variable $\hat{f}_n \in \{\pm 1\}$ expresses the similarity of the current and the previous data symbol, according to:

$$\hat{f}_n = \begin{cases} 1 & d_n = d_{n-1} \\ -1 & \text{else.} \end{cases}$$

The boxcar function $\Pi_{nT_s, (n+1)T_s}(t)$ indicates the variation in the symbol period T_s . It shall be emphasized, that the mean ranging bias \bar{b} and the deviation Δb , strongly depend on the specific code sequence and thus need to be determined numerically.

As long as the mean ranging bias is in the linear range of the S-curve

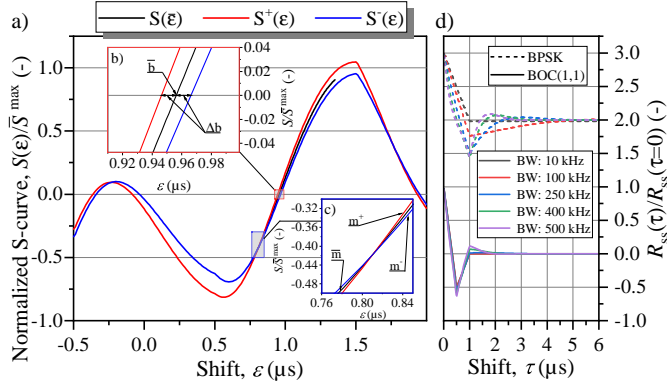


Fig. 4. In panel a), the S-curves S^+ (red curve) and S^- (blue curve), denoting whether the current and previous data symbol exhibit the same (+) or opposite (-) value, are depicted for an exemplary BPSK-modulated chip sequence. Moreover, in the linear range the mean S-curve, corresponding to the mean shift $\bar{\varepsilon}$, is illustrated by the black curve. All S-curves are normalized to the maximum of the mean value $\bar{S}(\varepsilon) = (S^+(\varepsilon) + S^-(\varepsilon))/2$. Panel b) shows the area at the zero crossing, indicating the parameters \bar{b} and Δb . Finally, panel c) portrays the slope variation between the S-curves S^+ and S^- , indicating the parameters \bar{m} , m^+ and m^- . Panel d) shows the normalized autocorrelation R_{ss} for an uncorrelated chip sequence filtered by a high-pass, representing the error transfer function of the PLL, at different filter bandwidths (BW). The results are depicted for BPSK- and BOC(1,1)-modulated sequences, indicated by the dashed and solid lines, respectively. Thereby, the former is offset by $R_{ss}(\tau)/R_{ss}(0) = 2$ for clarity.

it only constitutes the tracking point of the DLL, which can be accounted for by means of calibration and is thus omitted for further discussion. In contrast, the variation of the ranging bias confines the accuracy of the tracking loop. In order to identify the corresponding noise contribution, one can use Eq. 2 which describes the stochastic noise of BPSK modulation for the PLL, and apply it instead to the DLL analyzed in this section, by establishing a correspondence between the following parameters: $m_{\text{prn}} \rightarrow \Delta b$, $\hat{X}_n \rightarrow \hat{f}_n$, $T_c \rightarrow T_s$, leading to a noise spectral density of

$$N_b(f) = \Delta b^2 T_s \text{sinc}^2(\pi f T_s).$$

This noise spectral density is low-pass filtered within the DLL, followed by a read-out filter. Approximating both filters as an ideal low-pass filter, the variance at the read-out is given by:

$$\begin{aligned} \sigma_b^2 &= \Delta b^2 \int_{-B_F^d}^{B_F^d} T_s \text{sinc}^2(\pi f T_s) df, \\ &\approx 2\Delta b^2 B_F^d T_s. \end{aligned} \quad (18)$$

Thereby, B_F^d indicates the read-out filter bandwidth of the DLL, which is assumed to be much smaller than the inverse of the symbol period and smaller or equal to the bandwidth of the DLL low-pass filter. The error of the DLL is usually considered in terms of a ranging error. Thus, the code-tracking error $\sigma_{r,a}$ of this semi-analytical model will be defined as $\sigma_{r,a} = c\sigma_b$, where c denotes the speed of light. Similar expressions for the code-tracking error as stated in Eq. 18 have been found for alternative DLL implementations [5].

3.3 Application and numerical verification

Analogous to carrier tracking, also for code tracking numerical simulations have been conducted comparing BPSK and BOC(1,1) modulation

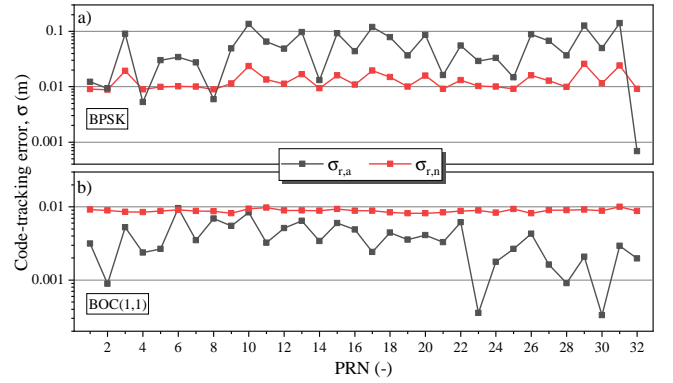


Fig. 5. The code-tracking error of a numerical DLL simulation (red data points) and a semi-analytical model (gray data points) is depicted for 32 randomly generated PRN sequences. In panel a) results are displayed for BPSK-modulated PRN sequences, while panel b) illustrates the outcome for BOC-modulated sequences.

schemes and verifying the semi-analytical model for the code-tracking error $\sigma_{r,a}$, cf. Eq. 18. Besides the baseline parameters as specified in Tab. 1, a set of 32 randomly generated PRN sequences has been considered. In terms of the semi-analytical code-tracking error $\sigma_{r,a}$, BOC(1,1) modulation displays a superior performance, differing by around one order of magnitude compared to the BPSK modulation, cf. gray data points in Fig. 5 a) and b). This result is expected: as explained in section 2, the BPSK modulation holds its peak spectral energy at the origin, leading to maximum damping due to the high-pass filter behavior of the error transfer function of the PLL. On the other hand, the spectral energy of the BOC(1,1) modulation is shifted away from the carrier, yielding less spectral confinement, cf. Fig. 2 a), and hence less distorted PRN sequences, see Fig. 3 a) [11]. Consequently, the S-curve of the BOC(1,1) modulation exhibits a smaller ranging bias variation Δb as well as an absolute ranging bias \bar{b} that is smaller by approximately two orders of magnitude.

The code-tracking error $\sigma_{r,n} = c\sqrt{\text{var}(\varepsilon)}$ of the numerical DLL simulation is based on the variance $\text{var}(\cdot)$ of the time shift ε , once the DLL has been settled. Interestingly, a significant deviation between modeled and simulated code-tracking errors is visible irrespective of the modulation scheme. For BOC(1,1) modulation the numerical code-tracking error is nearly constant over the set of PRN sequences, exhibiting a value of $\sigma_{r,n} \approx 9$ mm, cf. red data points in Fig. 5 panel b). Moreover, a correlation to the semi-analytical model is not evident at first glance. Although the code-tracking error of the model and the simulation are clearly correlated for BPSK modulation, see red data points in Fig. 5 panel a), deviations are still apparent in terms of the amplitude of the code-tracking error.

These deviations are attributed to the granularity of the PRN code generator and the varying slopes of the S-curves. The resolution of the PRN code generator is confined by the sampling rate of the incoming chip sequence. For BOC(1,1) modulation the sampling rate of 80 MHz cannot resolve the ranging bias variations. Consequently, simulations exhibit equal code-tracking errors, irrespective of the PRN sequence. The increased ranging bias variation for the BPSK modulation leads to a noticeable influence of the bias variation and hence establishes a correlation between the semi-analytical model and the simulation. Still, the variations are not fully resolved by the sampling rate. In addition, the slope m of the S-curves, necessary for the detection of the time shift ε , may yield an additional discrepancy. The DLL deduces the time shift based on the discriminator gain and thus implying a constant

S-curve slope, as delineated in section 3.1. Because the slopes m^\pm in the linear range of the S-curves S^\pm are not identical, see Fig. 4 c), the TOA estimation induces an error. In fact, analysis revealed that for the set of parameter values considered, the dominant error results from the sampling.

Nonetheless, both modulation schemes are capable of achieving sub-meter ranging errors, which is considered sufficient. Thereby, the BOC(1,1) modulation surpasses but at least equals the performance of the BPSK modulation.

At this point, it shall be emphasized, that due to the specific TOA detection, pure analytical analysis for the DLL is much more complex compared to the PLL. In particular, this applies to common simplifications, e.g. performed by Betz [5] (or further ones not shown here), which are not applicable in this context. These findings reinforce the necessity of numerical analysis for distinct code sequences and receiver architectures.

4 Conclusion

This paper revealed the compelling influence of the modulation scheme on the performance of sequential carrier- and code-tracking receiver architectures foreseen for future space-borne metrology systems.

A generic sequential PLL–DLL design including a representative signal consisting of a carrier modulated by code sequences has been introduced, enabling an analysis of the performance losses resulting exclusively from the architecture itself. Thereby, carrier and code tracking analyses have been conducted separately. In the former case a generic model has been introduced, exploiting the distinct parameter range and estimating the phase noise for an arbitrary but periodic modulation scheme. Thereby, the PSD of the pulse modulation within the read-out bandwidth has been identified as the main driver for phase noise. This model, subjected to BPSK and BOC(1,1) modulation revealed the superior phase noise performance of the latter. Moreover, it excluded BPSK as a modulation scheme for space-borne metrology systems demanding picometer phase noise levels, considering the stated set of parameter values. Finally, these results have been verified by numerical PLL simulations, which agreed well with the analytical model regardless of the modulation scheme.

Analysis of the code tracking has been focused on the TOA estimation, taking into account the concept of the S-curve. Thereby, a varying S-curve due to the PLL filtering of the incoming signal has been observed, differing in shape and zero crossing from the ideal case. Remarkably, analyses revealed that variations of the S-curve can be reduced to two cases, depending on whether the current and previous data symbols exhibit the same or opposite value, enabling a similar mathematical approach for the code tracking as used before for the phase noise. Finally, the model was compared with numerical DLL simulations. Differences became apparent, which were primarily attributed to the granularity of the PRN code generator. While both modulation schemes exhibited sub-meter ranging errors, BOC(1,1) modulation surpasses but at least equals the performance of the BPSK modulation.

Sequential carrier and code tracking architectures are thus in principle capable of serving as receivers for high-precision space-borne measurement systems, but performance is significantly affected by the modulation scheme. While the analysis was restricted to one data symbol per PRN sequence, it can easily be extended to analyses of PRN sequences exhibiting multiple data symbols, facilitating higher data rates.

Funding

Max-Planck-Institut für Gravitationsphysik (Albert-Einstein-Institut); Deutsches Zentrum für Luft- und Raumfahrt; Bundesministerium für

Wirtschaft und Klimaschutz (50 OQ 1801).

Acknowledgments

The authors thank T. Ziegler and S. Delchambre for their support and fruitful discussions.

Disclosures

The authors declare no conflicts of interest.

References

- [1] Klaus Abich, Alexander Abramovici, Bengie Ampan, Andreas Baatzsch, Brian Bachman Okihiro, David C Barr, Maxime P Bize, Christina Bogan, Claus Braxmaier, Michael J Burke, et al. In-orbit performance of the Grace Follow-On laser ranging interferometer. *Physical review letters*, 123(3):031101, 2019.
- [2] John W. Betz. Design and performance of code tracking for the gps m code signal. 2000.
- [3] John W. Betz. Binary offset carrier modulations for radionavigation. *NAVIGATION*, 48(4):227–246, 2001.
- [4] John W. Betz. Effect of linear time-invariant distortions on rns code tracking accuracy. 2002.
- [5] John W. Betz and Kevin R. Kolodziejwski. Generalized theory of code tracking with an early-late discriminator part i: Lower bound and coherent processing. *IEEE Transactions on Aerospace and Electronic Systems*, 45(4):1538–1556, 2009.
- [6] Karsten Danzmann, Thomas A Prince, et al. LISA assessment study report (yellow book). Technical Report ESA/SRE(2011)3, European Space Agency, February 2011.
- [7] Karsten Danzmann and the LISA Study Team. LISA—an ESA cornerstone mission for the detection and observation of gravitational waves. *Advances in Space Research*, 32(7):1233–1242, 2003.
- [8] EESA. LISA Metrology System. Technical Report ESA ITT AO/1-6238/10/NL/HB, 2014.
- [9] Juan José Esteban, Iouri Bykov, Antonio Francisco García Marín, Gerhard Heinzel, and Karsten Danzmann. Optical ranging and data transfer development for LISA. *Journal of Physics: Conference Series*, 154, 2009.
- [10] Juan José Esteban, Antonio F. García, Simon Barke, Antonio M. Peinado, Felipe Guzmán Cervantes, Iouri Bykov, Gerhard Heinzel, and Karsten Danzmann. Experimental demonstration of weak-light laser ranging and data communication for LISA. *Opt. Express*, 19(17):15937–15946, Aug 2011.
- [11] Juan José Esteban Delgado. *Laser Ranging and Data Communication for the Laser Interferometer Space Antenna*. PhD thesis, 2012.
- [12] Floyd M. Gardner. *Phaselock Techniques*. John Wiley & Sons, Inc., Hoboken, New Jersey, 3 edition, 2005.
- [13] Roger Haagsmans, Christian Siemes, Luca Massotti, Olivier Carraz, and Pierluigi Silvestrin. Esa’s next-generation gravity mission concepts. *Rendiconti Lincei. Scienze Fisiche e Naturali*, 31:15–25, 2020.
- [14] Gerhard Heinzel, Juan José Esteban, Simon Barke, Markus Otto, Yan Wang, Antonio F Garcia, and Karsten Danzmann. Auxiliary functions of the LISA laser link: ranging, clock noise transfer and data communication. *Classical and Quantum Gravity*, 28(9):094008, 2011.
- [15] Niklas Houba, Simon Delchambre, Tobias Ziegler, Gerald Hechenblaikner, and Walter Fichter. Lisa spacecraft maneuver design to estimate tilt-to-length noise during gravitational wave events. *Physical Review D*, 106(2):022004, 2022.

- [16] Seiji Kawamura, Masaki Ando, Naoki Seto, Shuichi Sato, Mitsuru Musha, Isao Kawano, Jun'ichi Yokoyama, Takahiro Tanaka, Kunihiro Ioka, Tomotada Akutsu, et al. Current status of space gravitational wave antenna decigo and b-decigo. *Progress of Theoretical and Experimental Physics*, 2021(5):05A105, 2021.
- [17] Ziren Luo, Yan Wang, Yueliang Wu, Wenrui Hu, and Gang Jin. The Taiji program: A concise overview. *Progress of Theoretical and Experimental Physics*, 2020.
- [18] Jianwei Mei, Yan-Zheng Bai, Jiahui Bao, Enrico Barausse, Lin Cai, Enrico Canuto, Bin Cao, Wei-Ming Chen, Yu Chen, Yan-Wei Ding, et al. The tianqin project: current progress on science and technology. *Progress of Theoretical and Experimental Physics*, 2021(5):05A107, 2021.
- [19] Martina Muratore, Daniele Vetrugno, and Stefano Vitale. Revisitation of time delay interferometry combinations that suppress laser noise in LISA. *Classical and Quantum Gravity*, 37(18):185019, 2020.
- [20] Donald R. Stephens. *Phase-Locked Loops for Wireless Communications: Digital and Analog Implementation*. Springer New York, NY, 2002.
- [21] Andrew Sutton, Kirk McKenzie, Brent Ware, and Daniel A Shaddock. Laser ranging and communications for LISA. *Optics Express*, 18(20):20759–20773, 2010.
- [22] Massimo Tinto and Sanjeev V Dhurandhar. Time-delay interferometry. *Living Reviews in Relativity*, 24(1):1–73, 2021.
- [23] A. J. Van. Theory and performance of narrow correlator spacing in a gps receiver. 1992.